Strain effects on spinodal decomposition in TiO_2-VO_2 films on TiO_2(100) substrates

Yuji Muraoka[a,*], Fumiya Yoshii[b], Takahiro Fukuda[b], Yuji Manabe[b], Mikiko Yasuno[b], Yoshito Takemoto[b], Kensei Terashima[a,**], Takanori Wakita[a], and Takayoshi Yokoya[a]

[a]Research Institute for Interdisciplinary Science, Okayama University, 3-1-1 Tsushima-naka, Tsushima, Kita-ku, Okayama 700-8530, Japan
[b]Graduate School of Natural Science and Technology, Okayama University, 3-1-1 Tsushima-naka, Tsushima, Kita-ku, Okayama 700-8530, Japan

[*] Corresponding author.
E-mail address: ymuraoka@cc.okayama-u.ac.jp

[**]Present address: International Center for Material Nanoarchitectonics (MANA), National Institute for Material Science (NIMS), 1-2-1 Sengen, Tsukuba, Ibaraki 305-0047, Japan

Abstract

We investigate the influence of lattice strain in the *c*-axis direction on spinodal decomposition in rutile TiO_2-VO_2 films on TiO_2(100) substrates. The [100]-oriented $Ti_{0.4}V_{0.6}O_2$(TVO) solid-solution films are fabricated on rutile TiO_2(100) substrates using a pulsed laser deposition with a KrF excimer laser, and are annealed inside the spinodal region. X-ray diffraction and scanning transmission electron microscopy are employed for characterization. Consequently, the in-plane tensile strain in the *c*-axis direction promotes the Ti-V interdiffusion in TVO/TiO_2(100) under thermal annealing. In contrast, relaxation of the tensile strain results in the occurrence of spinodal decomposition along the *c*-axis direction in the film. These results indicate that the relaxation of the tensile strain in the *c*-axis direction is critically important for enabling spinodal decomposition in TVO/TiO_2(100). Our work helps deepen the understanding of spinodal decomposition in the TVO film and provides information on achieving novel nanostructures via spinodal decomposition in TVO/TiO_2(100).

Keywords: Strain effect; Spinodal decomposition; Titanium dioxide; Vanadium dioxide; Thin films; Interdiffusion; Nanostructure; Pulsed laser deposition

1. Introduction

There has been considerable interest in the spontaneous formation of multilayer films via nanoscale phase separation in oxide systems [1-6]. In particular, interest has been focused on vertical multilayer (VML) films in which the multilayer structures are aligned vertically on the surface of the substrate. This is because VML films have great advantages over conventional multilayer films (horizontally aligned layers) in terms of easy interface probing, large interface area, and strain tunability to large thickness [5], and they provide opportunities to create new, self-assembled device architectures and multi-functionalities. There are several studies of the spontaneous formation of vertical nanostructures, such as nanopillars in $BaTiO_3/CoFe_2O_4$ [7] and nanocolumns in $BiFeO_3/Sm_2O_3$ and $BiFeO_3/Fe_3O_4$ [8,9]. However, few examples of VML films have been reported. There are significant requirements to achieving VML films. One is to determine the mechanism for forming well-ordered multilayer structures on the surface of the substrate. Another is to understand the influence of lattice strain on phase separation. This is because lattice strain can change the thermodynamic stability in phase-separated systems [10-12].

Spinodal decomposition is a phase-separation process in which a material spontaneously decomposes into two phases with distinct compositions. It leads to the spontaneous formation of microstructures with compositional fluctuations at the nanometer scale. Recently, it was reported that the rutile-type TiO_2-VO_2 bulk system exhibits spinodal decomposition [13-15]. VO_2 is known to exhibit a metal-insulator transition (MIT) at 340 K upon cooling, accompanied by a structural change from a high-temperature rutile-type tetragonal form to a low-temperature monoclinic form (M1) [16]. The TiO_2-VO_2 system shows a characteristic phenomenon, i.e., anisotropy in decomposition. When solid solutions of tetragonal-form $Ti_{0.4}V_{0.6}O_2$(TVO) are annealed below 800 K, phase decomposition occurs along the *c*-axis direction, and a nanometer-scale lamellar structure with alternating stacking of tetragonal Ti-rich and monoclinic V-rich phases is formed while retaining a coherent interface. The fluctuation in unidirectional composition is considered to be responsible for the smallest elastic free energy occurring in the *c*-axis direction [15,17,18].

Very recently, the anisotropy in decomposition has been applied to form multilayers in TVO films [19-23]. Chen *et al.* successfully obtained VML structures in epitaxial films [20]. They fabricated [100]-oriented TVO solid-solution films grown epitaxially on TiO_2(100) substrates. After the annealing of the films, vertically aligned lamellae were achieved through decomposition along the *c*-axis direction. The lamella periodicity was approximately 20 nm. This study showed that the anisotropy in decomposition is a significant advantage in achieving the spontaneous formation of VML structures in TVO/TiO_2(100). Regarding strain effects, previous studies have shown that the expanded in-plane *a*-axis length in the tetragonal lattice

does not significantly influence on the occurrence of spinodal decomposition in TVO films [22]. However, there has been no report of the strain effects in the *c*-axis direction on decomposition in TVO films. Because the decomposition occurs along the *c*-axis direction in TVO, the in-plane *c*-axis strain should affect the thermodynamic stability of the TVO system. It is, therefore, critically important to understand the strain effects on spinodal decomposition in TVO/TiO_2(100). Results help not only to deepen the understanding of the spinodal decomposition in the TVO film but also to establish a method to form the unique nanostructure of vertically aligned multilayer structures in TVO/TiO_2(100).

In this study, we examine the influence of the lattice strain in the *c*-axis direction on phase decomposition in [100]-oriented TVO epitaxial films on TiO_2(100) substrates. For this purpose, we prepare two types of films with thicknesses of 60 and 260 nm, using a pulsed laser deposition technique. In the 60-nm-thick film, the *c*-axis length is expanded due to the in-plane tensile strain in the *c*-axis direction to match the TiO_2 lattice constant. In the 240-nm-thick film, the tensile strain is relaxed in most of the film, while remaining in a small part of the film. These films are annealed at 673 K up to 540 h and characterized by X-ray diffraction (XRD), reciprocal space mapping (RSM), and scanning transmission electron microscopy (STEM). From the experimental results, we determine the importance of the relaxation of the tensile strain in the *c*-axis direction for the occurrence of spinodal decomposition in TVO/TiO_2(100). The relationship between the lamella periodicity and Ti content for the 260-nm-thick film is also examined. Finally, the results are explained from the viewpoint of energy considerations.

2. Experimental details

Solid-solution films oriented along the (100) plane were fabricated on TiO_2(100) substrates using a pulsed laser deposition method with a KrF excimer laser (λ = 248 nm). A target sample for TVO films was prepared via a normal solid-state reaction using rutile TiO_2 (99.99 %, rare metallic) and V_2O_3. V_2O_3 was obtained by reducing V_2O_5 (99.99%, rare metallic) under 5% H_2/Ar atmosphere at 1173 K. TiO_2 and V_2O_3 powders were mixed thoroughly with the molar ratio of Ti : V = 4 : 6. A pellet of the mixture was sintered at 1173 K for 12 h under an atmosphere of 5% H_2/Ar, and, subsequently, cooled to 300 K at a rate of 300 K/h. To prepare $Ti_{0.4}V_{0.6}O_2$ films, the substrate temperature was set to 673 K, and the oxygen pressure was maintained at 0.1 Pa. The deposition time was 0.5 h with a repetition rate of 1 Hz, increasing to 24 h with a repetition rate of 10 Hz. When the deposition was completed, the heater was turned off, and the films were cooled to 300 K under the same pressure. The laser fluence was 1.0 J/cm^2.

Table 1 shows the *a*- and *c*-axis lengths of TVO and TiO_2 in tetragonal form, together with the corresponding lattice mismatch. The *a*- and *c*-axis lengths of TVO are smaller than

those of TiO_2. This means that when a [100]-oriented TVO film is grown epitaxially on TiO_2(100), the in-plane *ac* lattice should be expanded due to the in-plane tensile strain at the interface. The lattice mismatches for the *a*- and *c*-axes are 0.81%, and 1.23%, respectively. The critical thickness calculated using the model of People and Beans [24] is 322 nm for the *a*-axis length and 76 nm for the *c*-axis length. With reference to these values, we prepared two types of films with thicknesses of 60 and 260 nm. These thicknesses were chosen to straddle the expected critical thickness for the *c*-axis length, below which the film is strained in the *c*-axis direction to match the substrate lattice constant and above which the film starts to be relaxed. Meanwhile, the in-plane *a*-axis is expected to be strained in the 60- and 260-nm-thick films because the thicknesses of two films are below the critical thickness for the *a*-axis length. Strictly speaking, the in-plane and out-of-plane *a*-axes are not equivalent in epitaxial TVO/TiO_2(100), because the tetragonal TVO lattice is deformed owing to the epitaxial strain in the in-plane *a*- and *c*-axes directions. However, we do not distinguish between these differences in this study and use the notations of in-plane and out-of-plane *a*-axes for simplicity.

The thickness of the films was determined using X-ray reflectivity measurements and TEM observations. Epitaxial growth of the film on the TiO_2(100) substrate is confirmed by X-ray ϕ scans. To induce spinodal decomposition, thermal annealing was performed at 673 K and an oxygen pressure of 0.1 Pa for up to 540 h. The films were examined using XRD and RSM measurements with monochromated Cu-Kα radiation (Rigaku Smart Lab-Pro). The TEM and STEM observations were performed at an accelerating voltage of 200 kV using a JEM-2100F (JEOL) electron microscope equipped with a Cs corrector and energy dispersive X-ray (EDX) analyzer (JED-2300). The specimens for TEM were prepared using the focused ion beam technique.

3. Results and discussion

3.1. TVO solid-solution films (60 and 260 nm thick) on TiO_2(100) substrates

Figure 1(a) shows the XRD patterns of 60- and 260-nm-thick TVO films on TiO_2(100) substrates. For both films, (200) and (400) diffractions of the TVO solid solution are observed and no other peaks apart from those from TVO and TiO_2 substrate are detected. These indicate that the two films are the [100]-oriented single phase of TVO solid solution. Figure 1(b) shows the XRD patterns near the (200) diffraction for the 60- and 260-nm-thick films. For the 60-nm-thick film, the (200) diffraction peak is observed at 2θ = 39.80°. The corresponding *d*-value is determined to be 0.2265 nm. This value is smaller than the TVO bulk value (0.2278 nm) [13,15], which is plausible owing to the in-plane tensile strain induced by the lattice matching between films and substrate. For the 260-nm-thick film, the (200) diffraction peak is observed at 2θ = 39.72°. The corresponding *d*-value of 0.2269 nm is close to the bulk value.

This suggests that the in-plane tensile strain tends to be relaxed in the 260-nm-thick film. To examine the in-plane lattice matching between the film and substrate, the RSM measurements of 60- and 260-nm-thick TVO films on TiO_2(100) substrates are conducted.

Figures 2(a) and (b) show the RSM results of the (310) and (301) diffractions, respectively, for the 60-nm-thick TVO/TiO_2(100), together with the corresponding diffraction positions of TVO bulk for comparison. As seen in Figs. 2(a) and (b), the film has the same in-plane Q_{010} and Q_{001} values as the substrate. These show that the film is strained in the in-plane *a*- and *c*-axis directions. The out-of-plane *a*-axis length of the film is smaller than that of the bulk. This is because of the presence of the in-plane biaxial tensile stress in the film. Figures 2(c) and (d) show the results of RSM of the (310) and (301) diffractions, respectively, for the 260-nm-thick TVO/TiO_2(100). In Fig. 2(c), the well-strained (310) diffraction peak of the film is observed, indicating that the in-plane *a*-axis length of the film is constrained by the substrate throughout the entire film. In Fig. 2(d), the (301) diffraction of the film extends toward the bulk position, and the intense peak is observed at around Q_{001} = 3.42 nm^{-1}. The observed Q_{001} value is almost the same as the bulk value (3.421 nm^{-1}) [13,15]. A weak (301) diffraction peak is also seen above the diffraction spot of the substrate. These results indicate that the tensile strain in the *c*-axis direction is relaxed in most of the film while still remaining in a small part of the film. We consider for the 260-nm-thick film a simple picture in which the in-plane *c*-axis length is fully constrained near the interface and relaxed toward the surface. The in-plane and out-of-plane lattice parameters of the 60- and 260-nm-thick TVO solid-solution films determined from the RSM results are tabulated in Table 2. The results are qualitatively consistent with those expected from the critical thickness of the film. Notably, the as-grown films are stabilized as solid solutions owing to kinetic limitations in the nonequilibrium growth process. This solid solution, however, is metastable and will decompose into phase-separated structures by thermal annealing.

It is noted that when looking at carefully (301) diffraction spots of the film and substrate in Figs. 2(b) and (d), we can see the finite intensity along the out-of- plane direction between the two spots. This suggests that the Ti-V interdiffusion starts to occur during the film preparation. Such interdiffusion can change the interface composition to $Ti_xV_{1-x}O_2$, which results in lowering the effective misfit and weakening the epitaxial strain at the interface between film and substrate. However, since the observed intensity between the two spots is small, it is considered that the influence of the intermixing at the interface on the epitaxial strain is small in the solid solution films.

3.2. TVO films (60 and 260 nm thick) on TiO_2(100)substrates after thermal annealing

The 60-nm-thick TVO solid-solution film on TiO_2(100) is annealed at 673 K up to 300

h to induce spinodal decomposition. Figure 3 shows the RSM results of the (301) diffraction for film annealed with the duration of 0, 100, and 300 h. After annealing for 100 h, the (301) diffraction spot of the film shifts downward, almost merging with the substrate at 300 h. No indication of phase separation is detected. The results show that during thermal annealing, the Ti content in the film is increased, and the film composition changes near TiO_2. The increase in Ti content is due to the Ti-V interdiffusion between the TVO film and TiO_2 substrate [25]. Such an interdiffusion has not been previously reported for TVO/TiO_2(100) in which the strain in the *c*-axis direction is relaxed [20]. Therefore our result indicates that the tensile strain in the *c*-axis direction in the film has the effect of promoting interdiffusion in TVO/TiO_2(100).

The 260-nm-thick solid-solution film is thermally annealed at 673 K up to 540 h. Figures 4(a) and (b) show the RSM results of the (310) and (301) diffractions, respectively, for the film annealed for 540 h. As seen in Fig. 4(a), the (310) diffraction of the film maintains a single peak with the same Q_{010} value as that of the (310) diffraction of the substrate. Meanwhile, in Fig. 4(b), satellites appear on either side of the strain-relaxed (301) diffraction spot in the *c*-axis direction of the film. These indicate that the 260-nm-thick film exhibits spinodal decomposition along the *c*-axis direction while retaining the in-plane tensile strain in the *a*-axis direction. The spacing between the satellite and central main spot yields a modulation periodicity of approximately 18 nm, which is consistent with a previous study [20]. The present results show that the relaxation of the tensile strain in the *c*-axis direction is important in enabling the spinodal decomposition in TVO/TiO_2(100). It is also shown that the in-plane tensile strain in the *a*-axis direction does not have a significant influence on the occurrence of spinodal decomposition in the film. When looking carefully at the (301) diffraction of the film in Fig. 4(b), we can see the strained part in the *c*-axis direction. This is quite in contrast to the result of the 60-nm-thick film in which the strained part of the (301) diffraction almost merges into the substrate after annealing for 300 h. The results indicate that the interdiffusion between the film and substrate tends to be suppressed in the 260-nm-thick film compared with the 60-nm-thick film, possibly due to the presence of spinodally decomposed phases inside the TVO film.

3.3 Spinodal decomposition in the 260-nm-thick TVO/TiO_2(100)

The occurrence of spinodal decomposition is examined using electron microscopy. Figure 5(a) shows the STEM image and selected-area electron diffraction (SAED) pattern (inset) of the 260-nm-thick TVO/TiO_2(100) after annealing for 540 h. The incident beam is oriented parallel to the [010] axis of the film. From the STEM image, the total film thickness is determined to be 260 nm. As shown in the figure, the bright and dark bands are vertical to the substrate and alternate quasi-periodically along the *c*-axis direction. The interface between the

bright and dark bands is perpendicular to the *c*-axis, appearing as a line when incident electrons are parallel to the [010] zone axis. The lamella periodicity determined from the average thickness of the bright and dark bands is approximately 18 nm, which is in good agreement with the estimated value from the RSM results. STEM-EDX analysis of the films shows that Ti condenses in the dark bands and V in the bright bands as shown in Figs. 5(b) and (c). The composition profiles along the *c*-axis direction in Fig. 5(d) reveal antiphase modulations for Ti and V. The results show that the film consists of Ti-rich and V-rich lamellae, and clearly indicate that spinodal decomposition along the *c*-axis direction occurs in the film. The occurrence of spinodal decomposition in the film is further supported by the result of resistivity measurements shown in Appendix A.1.

When looking at the image near the interface, we find a different feature from inside the film. Figure 6(a) shows the STEM image near the interface in the film. As the interface is approached, the number of dark (Ti-rich) and bright (V-rich) bands decreases, and the dark bands widen. Near the interface, only the dark bands are left. This feature can be also seen in the composition profiles along the *c*-axis direction in Fig. 6(b). At 110 nm from the surface of substrate, the antiphase modulations for Ti and V are observed, and the lamella periodicity is approximately 18 nm. At 64 nm from the substrate, the antiphase modulation becomes less obvious, and the thickness of the Ti-rich layer is widened. The modulation period increases to approximately 31 nm. At 20 nm from the substrate, the antiphase modulation disappears, and the solid solution is present. The results indicate that near the interface, spinodal decomposition is less likely to occur, and the solid solution is stabilized. In Table 3, the lamella periodicity at the distance from the substrate is tabulated.

We consider that near the interface, the film composition is altered due to the Ti-V interdiffusion in TVO/TiO_2(100). Figure 7(a) (left-side axis) displays the composition profile along the out-of-plane *a*-axis direction in the film, which is obtained from the analysis of the STEM image in the film. It is observed that inside the film, the Ti content increases toward the interface. From the film surface down to approximately 100 nm, the Ti content remains unchanged with a value of 0.4. This value is consistent with the nominal value of the film ($Ti_{0.4}V_{0.6}$). Below 100 nm, Ti content starts to increase continuously, reaching a value of 0.73 at approximately 20 nm. The Ti content of 0.73 is almost unchanged from 20 to 0 nm (substrate). The results reveal that Ti-V interdiffusion occurs and extends to approximately 100 nm, near the interface in the film. Remember that the Ti-V interdiffusion in TVO/TiO_2(100) is enhanced by the presence of the tensile strain in the *c*-axis direction, as shown in Fig. 3. Therefore, it is considered that in the 260-nm-thick film, before annealing, the tensile strain is free from the surface of the film till 100 nm; however, the interdiffusion gradually increases from 100 to 20 nm, and is fully functional between 20 and 0 nm (substrate).

When plotting the lamella periodicity in Table 3 with respect to the distance from the substrate, an interesting feature can be seen; this feature corresponds to the periodicity changes with distance that are similar to the Ti content, as shown in Fig. 7(a) (right-side axis). The periodicity of approximately 18 nm is maintained from 260 nm to approximately 100 nm and subsequently increases toward the interface. There are two possible reasons for the increase in periodicity on the interface side. One is the decrease in the driving force of the spinodal decomposition due to the increase in strain energy [10,26]. Another is the increase in Ti content on the interface side. As seen in Figure 7(b), the lamella periodicity is plotted with respect to Ti content inside the film. The lamella periodicity tends to increase with increasing Ti content. This result indicates that the Ti content is an important factor in determining the lamella periodicity in the TVO film. These suggest that the lamella periodicity in the TVO film can be controlled by two parameters, which are the strain in the *c*-axis direction and Ti content.

Finally, we estimate the compositions of the Ti- and V-rich phases at the distances of 64 and 110 nm from the substrate. In this estimation, the intensity ratios of elemental Ti and V in each Ti- and V-rich layer are averaged. The results obtained are plotted in Figure 8. In the figure, the horizontal axis represents the Ti content, and the vertical axis represents the distance from the substrate. The result in Fig. 7(a) (left-side axis) is shown again in the same figure. As the distance changes from 110 to 64 nm, the Ti content evidently increases from 0.33 to 0.45 in the V-rich phase, whereas it changes slightly from 0.61 to 0.65 in the Ti-rich phase. The results show that the V-rich phase is difficult to precipitate near the interface. The Ti content of ~0.7 corresponds to the concentration near the phase boundary with the Ti-rich phase. This phase boundary composition is almost the same as that for the bulk [13].

3.4. Interpretation of the experimental results for 60- and 260-nm-thick TVO films on TiO_2(100) substrates

We interpret the experimental results of 60- and 260-nm-thick TVO films on TiO_2(100) substrates from the viewpoint of energy considerations. Here, we consider the influence of the in-plane tensile strain in the *c*-axis direction only, because the expanded *a*-axis length does not have a significant effect on the occurrence of the decomposition. In the 60-nm-thick solid-solution film, the in-plane *c*-axis length is expanded owing to the tensile strain in the *c*-axis direction to match that of TiO_2. The expansion of the *c*-axis length generates an elastic energy, resulting in the increase in the total energy of the film. This can lead to the loss of the driving force of the spinodal decomposition and stabilization of the solid-solution state in the film at the annealing temperature of 673 K [10-12]. During thermal annealing, the film remains in the solid-solution state and retains the expanded *c*-axis length with increasing Ti content via interdiffusion to obtain a lower effective misfit. Because the volume of TiO_2

substrate is much larger than that of the film, the film incorporates a considerable amount of Ti ions from the substrate to change the film composition close to that of TiO_2. Consequently, the elastic energy required to match the film to the expanded lattice of the substrate can be relieved, and the total energy in the system is reduced. The Ti diffusion from the substrate plays a role in reducing the elastic energy in the film. This is illustrated in Figure 9(a).

For the 260-nm-thick solid-solution film, the in-plane tensile strain in the *c*-axis direction is fully relaxed in most of the inside of the film (100-260 nm from the substrate). As there is no strain in the *c*-axis direction, the film lattice does not need to incorporate the Ti ions to reduce the elastic energy by annealing. In this region, the driving force of the spinodal decomposition is kept large, in which only the spinodal decomposition serves to lower the total energy [27].

In the region around the interface (20-100 nm from the substrate), the in-plane tensile strain in the *c*-axis direction gradually increases toward the interface. The increased elastic energy results in a decrease in the driving force of the spinodal decomposition. In this situation, both the interdiffusion and spinodal decomposition can be generated by thermal annealing. A certain amount of Ti ions is incorporated into the film via interdiffusion, depending on the degree of the tensile strain in the *c*-axis direction, which lowers the elastic energy. The spinodal decomposition also occurs to reduce the free energy in the film. Thus, both the incorporation of Ti ions and spinodal decomposition contribute to the energy reduction in this region.

Near the interface (0-20 nm from the substrate), the situation is the same as that for the 60-nm-thick film. The expansion of the in-plane *c*-axis length of the film produces an elastic energy, reducing the driving force of the spinodal decomposition. By thermal annealing, the solid-solution phase takes Ti ions from the substrate via the diffusion while maintain the expanded *c*-axis length to obtain a lower effective misfit. Near the interface, the film changes its composition to obtain a lower elastic energy. The picture for the 260-nm-thick film is shown in Figure 9(b).

We interpret the experimental results in terms of the energy considerations. It is also important to consider the effect of kinetics on the decomposition to better understand the results. Nevertheless, because the explanation above seems to be reasonable, our picture provides a good starting point to understand the influence of the lattice strain in the *c*-axis direction on the decomposition in TVO/TiO_2(100). Knowledge of the present work helps deepen the understanding of the spinodal decomposition in the TVO film. Regarding the VML formation, the strain relaxation in the *c*-axis direction is crucially important in the formation of VML structures via spinodal decomposition in TVO/TiO_2(100). Using buffer layers that function to relieve the lattice strain is effective in achieving VML structures. Buffer layers that act as

diffusion barriers for Ti ions are also effective. Our results provide helpful information in establishing a way to form VML structures via spinodal decomposition in TVO/TiO_2(100).

4. Conclusions

We examine the influence of the lattice strain along the *c*-axis direction on the spinodal decomposition in rutile TVO/TiO_2(100). Solid-solution [100]-oriented TVO films with thicknesses of 60 and 260 nm are fabricated on rutile TiO_2(100) substrates using a pulsed laser deposition with a KrF excimer laser; these films are characterized using X-ray diffraction and scanning transmission electron microscopy. In the 60-nm-thick film, the *c*-axis length is expanded due to the in-plane tensile strain in the *c*-axis direction to match the TiO_2 lattice constant. In the 260-nm-thick film, the tensile strain is relaxed in majority of the film while remaining in a small part of the film. These films are annealed inside the spinodal region. As a result, remarkable Ti-V interdiffusion occurs in the 60-nm-thick film, and the resultant film is the solid solution with a composition close to that of TiO_2. In the 260-nm-thick film, spinodal decomposition occurs in the strain-relaxed part inside the film, whereas the solid-solution phase remains near the interface. These results reveal that the in-plane tensile strain in the *c*-axis direction promotes interdiffusion; this indicates that the relaxation of the tensile strain in the *c*-axis direction is critically important for the enabling of spinodal decomposition in TVO/TiO_2(100). It is also shown that both strain in the *c*-axis direction and the Ti content are important parameters for determining the lamella periodicity in the TVO film. The obtained results can be reasonably explained in terms of energy considerations. Our work helps not only to deepen the understanding of the spinodal decomposition in the TVO film but also to establish a method to form the unique nanostructure of vertically aligned multilayer structures in TVO/TiO_2(100).

Acknowledgements

We would like to thank T. Koyama for useful discussion. This research was supported by JSPS KAKENHI Grant Number JP17K06794, and partially by the Program for Promoting the Enhancement of Research University from Ministry of Education, Culture, Sport, Science and Technology, Japan.

Appendix A.1. Resistivity of the prepared 260-nm-thick TVO/TiO_2(100) film before and after annealing

Resistivity measurements are performed via a standard four-probe method within a temperature range of 280 to 380 K using a physical property measurement system (Quantum Design). Figure A.1 shows the temperature dependence of resistivity for the 260-nm-thick

TVO/TiO_2(100) films before and after annealing at 673 K for 540 h. After annealing, the film shows a metal-insulator transition (MIT) at 339 K. The MIT temperature is considered the midpoint of the jump in the resistivity curve that is measured upon heating [28]. The MIT is a result of the presence of the V-rich phase in spinodally decomposed films, which supports the occurrence of the spinodal decomposition in the 260-nm-thick TVO/TiO_2(100) films after annealing. The transition temperature of the films is lower than those of [100]-oriented $Ti_xV_{1-x}O_2$ solid solution films grown on TiO_2(100) [29]. This suggests that the in-plane and out-of-plane *a*-axis lengths of the V-rich phase are expanded due to the tensile strain induced by the coherent interface between the Ti-rich phase and V-rich phase [28]. The result of resistivity measurements provides useful information about the strain between the TiO_2/VO_2 lamellar walls. Before annealing, the film is insulating although a sign of the MIT is observed. This implies that the spinodal decomposition starts to occur in the film before annealing, although there is no obvious sign of the decomposition in the results of the XRD measurements.

References

[1] S. Arakawa, K. Mogi, K. Kikuta, T. Yogo, S. Hirano, Y. Seki, M. Kawamoto, Phase separation of alkoxy-derived (Ti,Sn)O_2 oriented thin films, J. Am. Ceram. Soc. 80 (11) (1997) 2864-2868, https://doi.org/10.1111/j.1151-2916.1997.tb03204.x.

[2] S. Arakawa, K. Mogi, K. Kikuta, T. Yogo, S. Hirano, Y. Seki, Gas-sensing properties of spinodally decomposed (Ti,Sn)O_2 thin films, J. Am. Ceram. Soc. 82 (1) (1999) 225-228, https://doi.org/10.1111/j.1151-2916.1999.tb01749.x.

[3] J. Liu, X. Wu, W. N. Lennard, D. Landheer, Surface-directed spinodal decomposition in hafnium silicate thin films, Phys. Rev. B 80 (2009) 041403(R), https://doi.org/10.1103/PhysRevB.80.041403.

[4] H. Yang, H. Wang, B. Maiorov, J. Lee, D. Talbayev, M. J. Hinton, D. M. Feldmann, J. L. MacManus-Driscoll, A. J. Taylor, L. Civale, T. R. Lemberger, Q. X. Jia, Self-assembled multilayers and enhanced superconductivity in $(YBa_2Cu_3O_{7-x})_{0.5}$:$(BaZrO_3)_{0.5}$ nanocomposite films, J. Appl. Phys. 106 (9) (2009) 093914, https://doi.org/10.1063/1.3257238.

[5] J. L. MacManus-Driscoll, Self-assembled heteroepitaxial oxide nanocomposite thin film structures: Designing interface-induced functionality in electronic materials, Adv. Funct. Mater. 20 (13) (2010) 2035-2045, https://doi.org/10.1002/adfm.201000373.

[6] N. Wakiya, N. Sakamoto, S. Koda, W. Kumasaka, N. Debnath, T. Kawaguchi, T. Kiguchi, K. Shinozaki, H. Suzuki, Magnetic-field-induced spontaneous superlattice formation via spinodal decomposition in epitaxial strontium titanate thin films, NPG Asia Materials 8 (2016) e279, https://doi.org/10.1038/am.2016.76.

[7] H. Zheng, J. Wang, S. E. Lofland, Z. Ma, L. Mohaddes-Ardabili, T. Zhao, L. Salamanca-Riba, S. R. Shinde, S. B. Ogale, F. Bai, D. Viehland, Y. Jia, D. G. Schlom, M. Wuttig, A. Roytburd, R. Ramesh, Science 303 (5658) (2004) 661-663, https://doi.org/10.1126/science.1094207.

[8] J. L. MacManus-Driscoll, P. Zerrer, H. Wang, H. Yang, J. Yoon, A. Fouchet, R. Yu, M. G. Blamire, Q. Jia, Strain control and spontaneous phase ordering in vertical nanocomposite heteroepitaxial thin films, Nat. Mater. 7 (4) (2008) 314-320, https://doi.org/10.1038/nmat2124.

[9] E-M. Choi, E. Weal, Z. Bi, H. Wang, A. Kursumovic, T. Fix, M. G. Blamire, J. L. MacManus-Driscoll, Strong room temperature exchange bias in self-assembled BiFeO3-Fe3O4 nanocomposite heteroepitaxial films, Appl. Phys. Lett. 102 (1) (2013) 012905, https://doi.org/10.1063/1.4773567.

[10] D. J. Seol, S. Y. Hu, Y. L. Li, J. Shen, K. H. Oh, L. O. Chen, Computer simulation of spinodal decomposition in constrained films, Acta Materialia 51 (17) (2003) 5173-5185, https://doi.org/10.1016/S1359-6454(03)00378-1.

[11] W. C. Johnson, C. S. Chiang, Phase equilibrium and stability of elastically stressed heteroepitaxial thin films, J. Appl. Phys. 64 (3) (1988) 1155-1165, https://doi.org/10.1063/1.341878.
[12] C. S. Chiang, W. C. Johnson, Coherent phase equilibria in systems possessing a consolute critical point, J. Mater. Res. 4 (3) (1989) 678-687, https://doi.org/10.1557/JMR.1989.0678.
[13] Z. Hiroi, H. Hayamizu, T. Yoshida, Y. Muraoka, Y. Okamoto, J. Yamaura, Y. Ueda, Spinodal decomposition in the TiO_2-VO_2 system, Chem. Mater. 25 (11) (2013) 2202-2210, https://doi.org/10.1021/cm400236p.
[14] Z. Hiroi, T. Yoshida, J. Yamaura, Y. Okamoto, Spinodally decomposed nanostructures in a TiO_2-VO_2 crystal, APL Mater. 3 (6) (2015) 062508, https://doi.org/10.1063/1.4919764.
[15] M. Ogata, K. Kadowaki, M. Ijiri, Y. Takemoto, K. Terashima, T. Wakita, T. Yokoya, Y. Muraoka, Effect of aliovalent dopants on the kinetics of spinodal decomposition in rutile-type TiO_2-VO_2, J. Eur. Ceram. Soc. 37 (9) (2017) 3177-3183, https://doi.org/10.1016/j.jeurceramsoc.2017.03.039.
[16] F. J. Morin, Oxides which show a metal-to-insulator transition at the Neel temperature, Phys. Rev. Lett. 3 (1) (1959) 34-36, https://doi.org/10.1103/PhysRevLett.3.34.
[17] V. S. Stubican, A. H. Schultz, Phase separation by spinodal decomposition in the tetragonal system, J. Am. Ceram. Soc. 53 (4) (1970) 211-214, https://doi.org/10.1111/j.1151-2916.1970.tb12072.x.
[18] K. T. Wu, K. S. Mendelson, Spinodal decomposition in the tetragonal system, J. Chem. Phys. 58 (7) (1973) 2929-2933, https://doi.org/10.1063/1.1679600.
[19] G. Sun, H. Zhou, X. Cao, R. Li, M. Tazawa, M. Okada, P. Jin, Self-assembled multilayer structure and enhanced thermochromic performance of spinodally decomposed TiO_2-VO_2 thin film, ACS Appl. Mater. Interfaces 8 (11) (2016) 7054-7059, https://doi.org/10.1021/acsami.5b12476.
[20] Z. Chen, X. Wang, Y. Qi, S. Yang, J. A. N. T. Soares, B. A. Apgar, R. Gao, R. Xu, Y. Lee, X. Zhang, J. Yao, L. W. Martin, Self-assembled, nanostructured, tunable metamaterials via spinodal decomposition, ACS Nano 10 (11) (2016) 10237-10244, https://doi.org/10.1021/acsnano.6b05736.
[21] G. Sun, X. Cao, Y. Yue, X. Gao, S. Long, N. Li, R. Li, H. Luo, P. Jin, Multi-nanolayered VO_2/sapphire thin film via spinodal decomposition, Sci. Rep. 8 (1) (2018) 5342, https://doi.org/10.1038/s41598-018-23412-4.
[22] Y. Matsuura, F. Yoshii, T. Otsuka, K. Kadowaki, M. Ijiri, Y. Takemoto, K. Terashima, T. Wakita, T. Yokoya, Y. Muraoka, Multilayer formation via spinodal decomposition in TiO_2-VO_2 epitaxial films on sapphire substrates, J. Eur. Ceram. Soc. 38 (15) (2018) 5043-5050, https://doi.org/10.1016/j.jeurceramsoc.2018.07.035.

[23] J. Park, G-Y. Kim, K. Song, S-Y. Choi, J. Son, Self-assembly of correlated (Ti,V)O_2 superlattices with tunable lamella periods by kinetically enhanced spinodal decomposition, NPG Asia Materials 11 (1) (2019) 1-9, https://doi.org/10.1038/s41427-019-0132-z.
[24] R. People, J. C. Bean, Calculation of critical layer thickness versus lattice mismatch for Ge_xSi_{1-x}/Si strained-layer heterostructures, Appl. Phys. Lett. 47 (3) (1985) 322-324, https://doi.org/10.1063/1.96206.
[25] Y. Muraoka, K. Saeki, R. Eguchi, T. Wakita, M. Hirai, T. Yokoya, S. Shin, Spectroscopic evidence of the formation of (V,Ti)O_2 solid solution in VO_2 thinner films grown on TiO_2(001) substrates, J. Appl. Phys. 109 (4) (2011) 043702, https://doi.org/10.1063/1.3549835.
[26] J. W. Cahn, On spinodal decomposition, Acta Met. 9(9) (1961) 795-801, https://doi.org/10.1016/0001-6160(61)90182-1.
[27] J. W. Cahn, J. E. Hilliard, Free energy of a nonuniform system. I. Interfacial free energy, J. Chem. Phys. 28 (2) (1958) 258-267, https://doi.org/10.1063/1.1744102.
[28] Y. Muraoka, Z. Hiroi, Metal-insulator transition of VO_2 thin films grown on TiO_2(001) and (110) substrates, Appl. Phys. Lett. 80(4) (2002) 583-585, https://doi.org/10.1063/1.1446215.
[29] I. Balberg, B. Abeles, Y. Arie, Phase transition in reactive co-sputtered films of VO_2-TiO_2, Thin Solid Films 24(2) (1974) 307-310, https://doi.org/10.1016/0040-6090(74)90175-8.

Figure captions

Fig. 1. (a) XRD patterns of 60- and 260-nm-thick TVO solid-solution films grown on TiO_2(100) substrates. (b) Enlarged XRD patterns near $2\theta = 40°$ for the 60- and 260-nm-thick TVO films on TiO_2(100) substrates. The 2θ position of the (200) diffraction for TVO bulk [13,15] is also shown in the figure.

Fig. 2. Results of RSM of (a) (310) and (b) (301) diffractions for the 60-nm-thick TVO/TiO_2(100). Results of RSM of (c) (310) diffraction and (d) (301) diffraction for the 260-nm-thick TVO/TiO_2(100). In these figure, the (310) and (301) diffraction positions for TVO bulk are displayed with a cross mark (×) for comparison [13,15].

Fig. 3. Results of the (301) diffractions for the 60-nm-thick TVO/TiO_2(100) film before and after annealing at 673 K for 100 and 300 h .

Fig. 4. Results of RSM of (a) (310) and (b) (301) diffractions for the 260-nm-thick TVO/TiO_2(100) after annealing at 673 K for 540 h. The (310) and (301) diffraction positions for TVO bulk are also displayed.

Fig. 5. (a) Dark-field STEM image obtained at the [010] zone axis for the 260-nm-thick TVO film after annealing at 673 K for 540 h. The SAED pattern is shown in the inset of (a). The arrows denote the superlattice peaks arising from the monoclinic nature of the V-rich phase [20]. EDX elemental maps for (b) Ti is marked as red and (c) V as yellow in the annealed 260-nm-thick TVO(100) film. Dark bands in (a) contain more Ti/V content. (d) Line scans of the EDX elemental maps along the [001] direction (lateral direction) in the STEM image (a). Alternating variations of Ti and V contents are observed. The average wavelength is approximately 18 nm.

Fig. 6. (a) Dark-field STEM image around the interface obtained at the [010] zone axis for the 260-nm-thick TVO film after annealing at 673 K for 540 h. White dot lines show the position of the distance, 64 and 110 nm from the substrate surface. (b) Line scans of the EDX elemental maps along the [001] direction (lateral direction) in the STEM image (a) at the distance of (top) 110 and (bottom) 64 nm from the TiO_2 substrate.

Fig. 7. (a) (Left axis) Ti content profile along the out-of-plane *a*-axis direction in the 260-nm-thick TVO film after annealing at 673 K for 540 h. Horizontal axis is represented in

distance from the substrate. (Right axis) Lamella periodicity in Table 3 plotted with respect to the distance from TiO_2 substrate for the 260-nm-thick TVO film after annealing at 673 K for 540 h. (b) Lamella periodicity plotted with respect to the Ti content in the 260-nm-thick TVO film after annealing at 673 K for 540 h.

Fig. 8. Ti content in the Ti- (triangles) and V-rich (circles) phases for the 260-nm-thick TVO film after annealing at 673 K for 540 h. In the figure, a horizontal axis represents the Ti content in V- and Ti-rich phases, and a vertical axis represents the distance from the TiO_2 substrate to the film surface. Results of the Ti content at the distances of 64 and 110 nm are shown along with the Ti content of the solid solution phase near interface (square). The Ti content profile along the out-of-plane *a*-axis direction (black dot line) is shown in the figure again.

Fig. 9. (a) (Left) Schematic illustration of the 60-nm-thick film at 673 K. (Right) A simple picture of free energy with respect to Ti content at 673 K for the 60-nm-thick film. (b) (Left) Schematic illustration of the 260-nm-thick film at 673 K. (Right) Simple pictures of free energy with respect to Ti content at 673 K for the 260-nm-thick film.

Fig. A.1. Temperature dependence of resistivity for (a) the 260-nm-thick TVO/TiO_2(100) before and after annealing at 673 K for 540 h.

Table 1 Lengths of the *a*- and *c*-axis of $Ti_{0.4}V_{0.6}O_2$ and TiO_2 in tetragonal form. The lattice mismatch between $Ti_{0.4}V_{0.6}O_2$ and TiO_2 is presented.

Axis length / material	*a* / nm	*c* / nm
$Ti_{0.4}V_{0.6}O_2$ [13,15]	0.4556	0.2923
TiO_2	0.4593	0.2959
Lattice mismatch / %	0.81	1.23

Table 2 Lengths of the *a*- and *c*-axis of the 60- and 260-nm-thick TVO solid-solution films on TiO_2(100) substrates determined from the results of the reciprocal space mapping.

Axis length / film		Out-of-plane *a*-axis length / nm	In-plane *a*-axis length / nm	*c* / nm
60-nm-thick TVO		0.453	0.459	0.296
260-nm-thick TVO	Strained part	0.453	0.458	0.296
	Relaxed part	0.454	0.459	0.293

Table 3 Lamella periodicity vs. distance from the TiO_2 substrate for 260-nm-thick TVO/TiO_2(100) after annealing at 673 K for 540 h.

Distance from TiO_2 substrate / nm	Lamella periodicity / nm
36	32
64	31
90	25
110	18
124	17
180	19
233	19

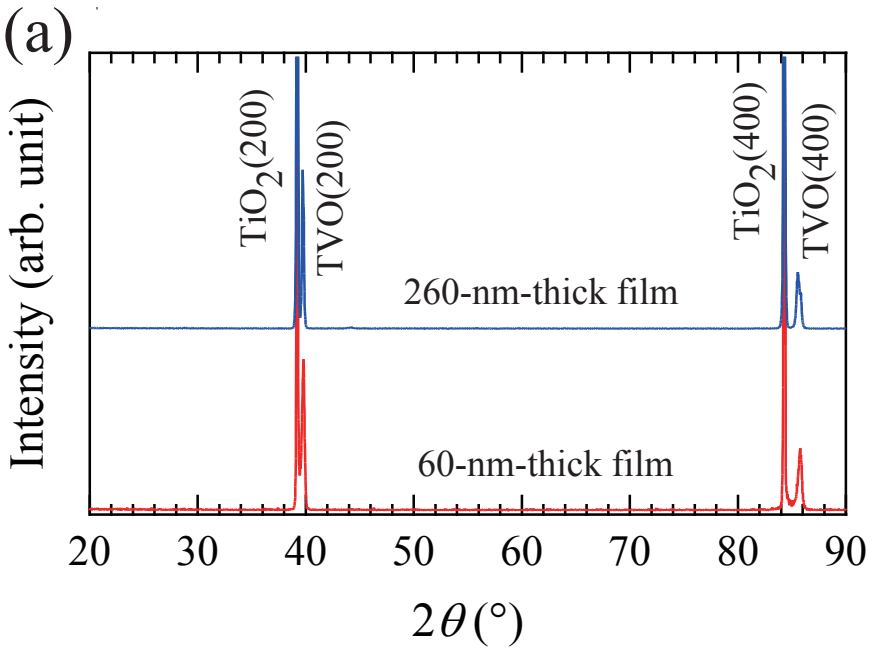

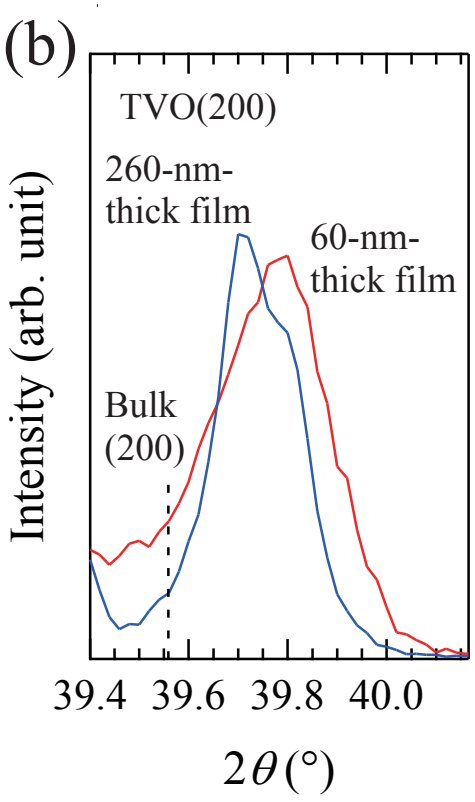

Figs. 1(a)(b). Y. Muraoka et al.

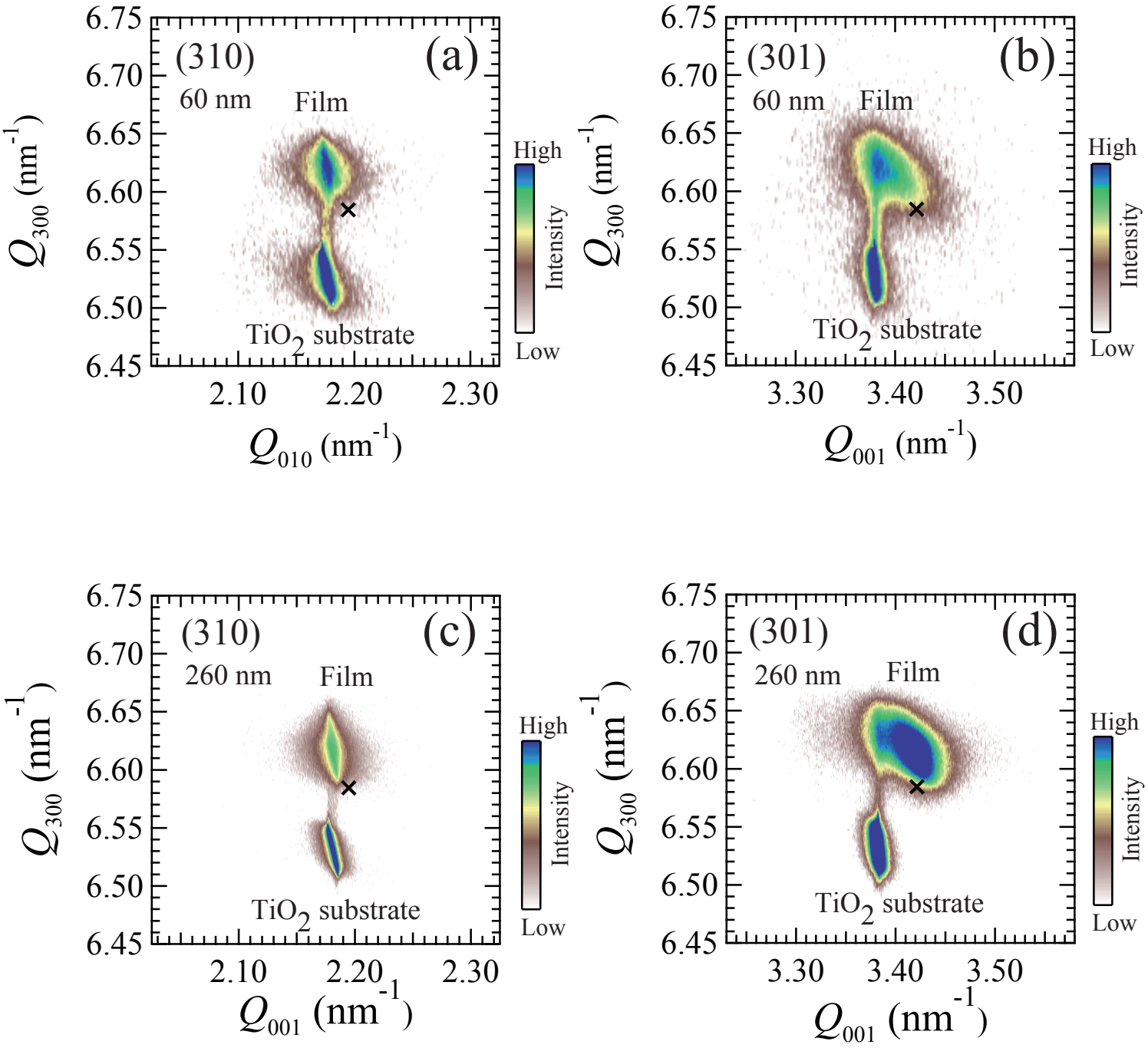

Figs. 2(a)(b)(c)(d). Y. Muraoka et al.

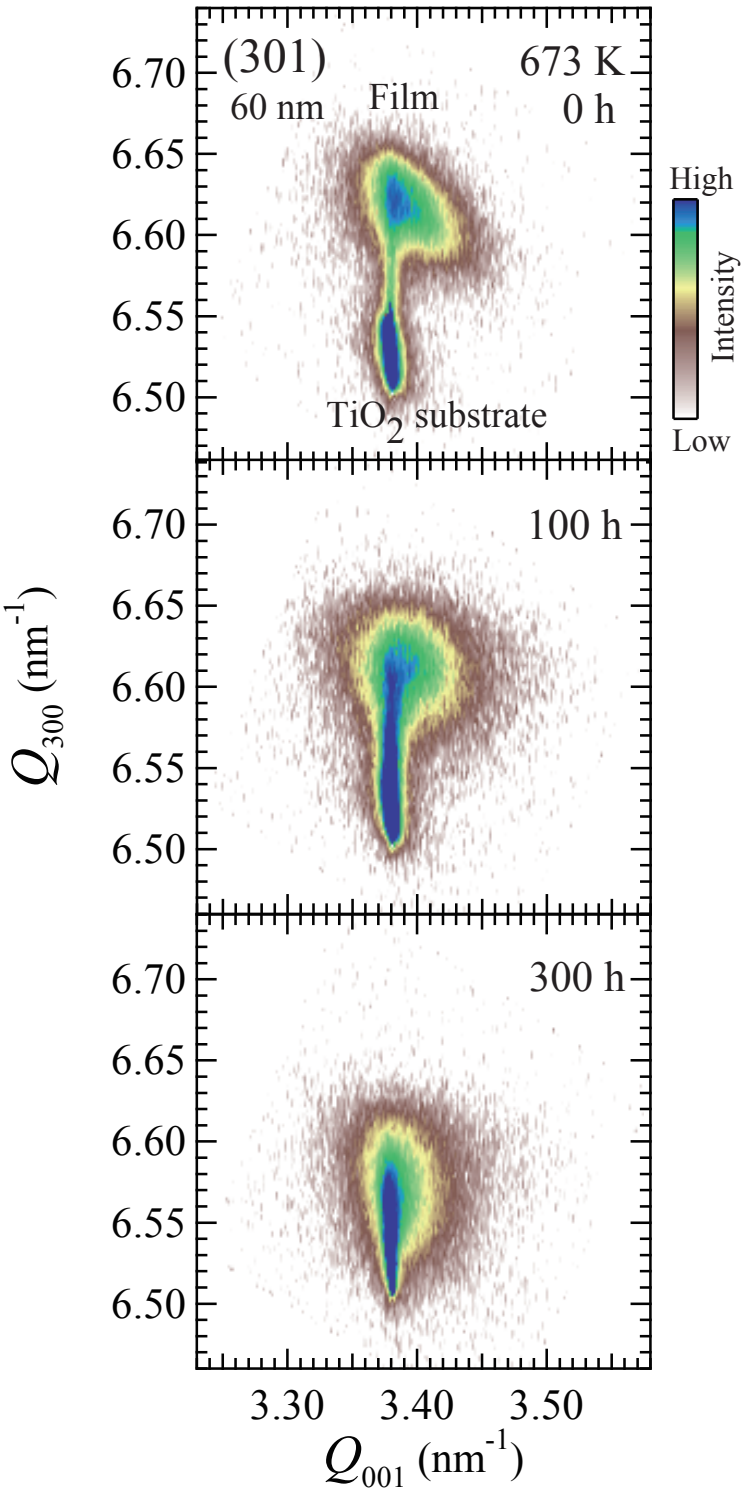

Fig. 3. Y. Muraoka et al.

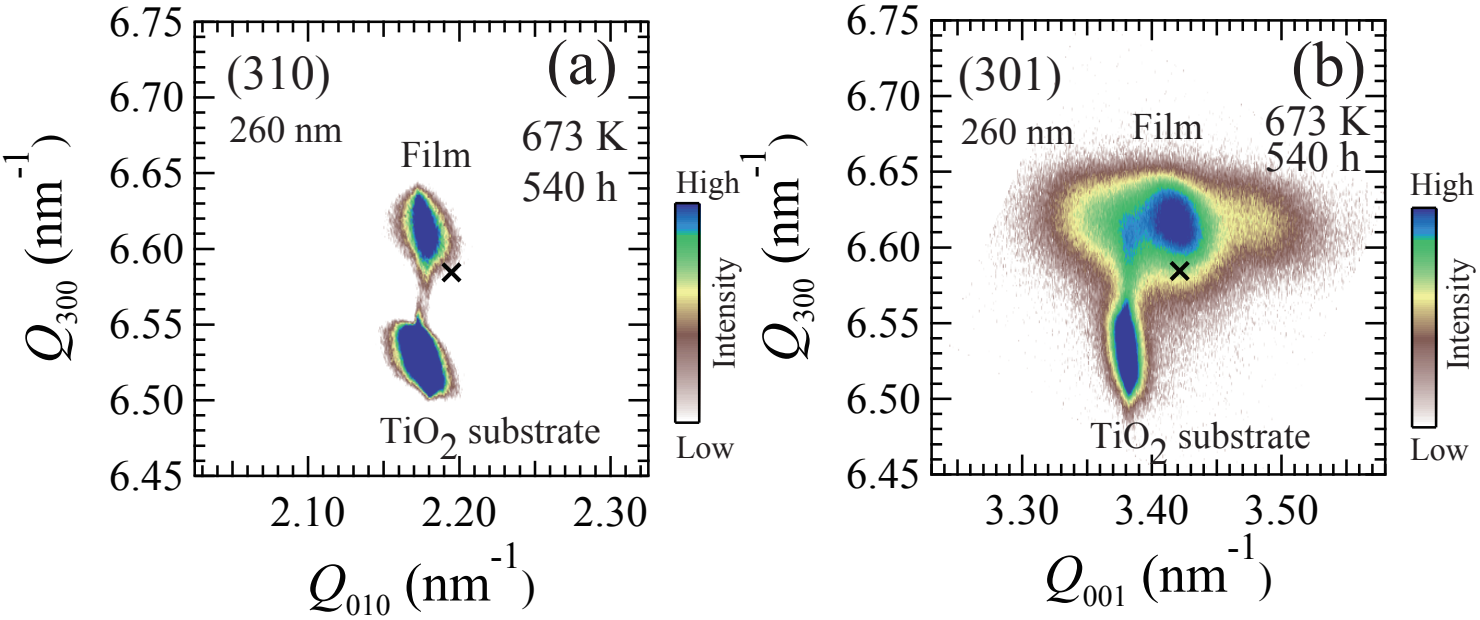

Figs. 4(a)(b). Y. Muraoka et al.

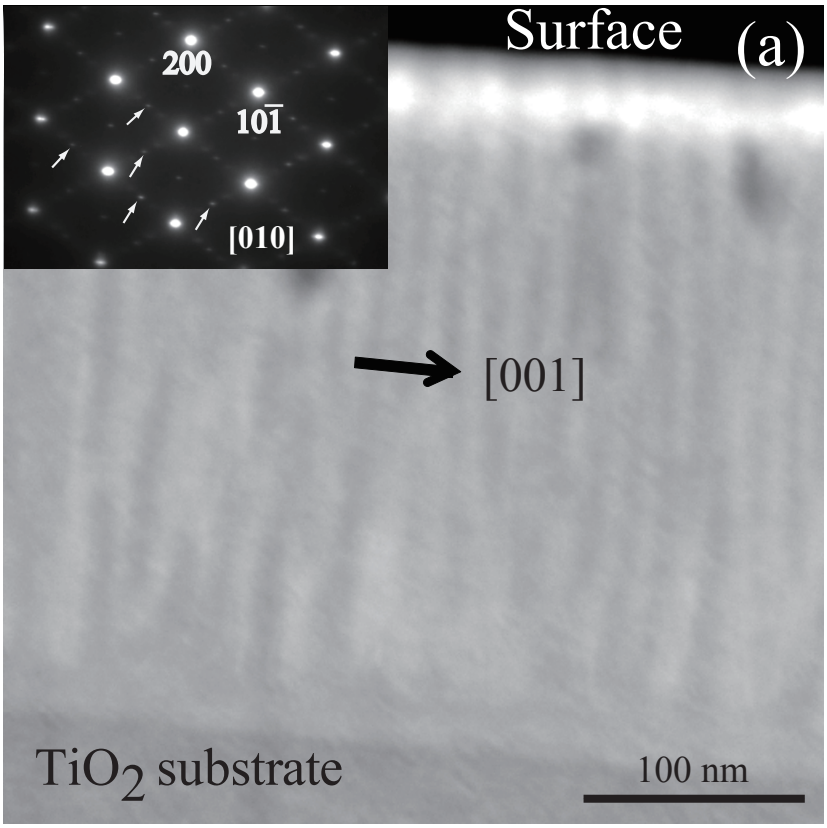

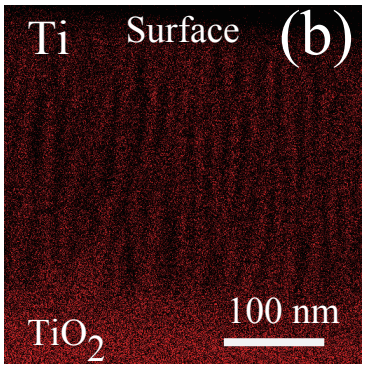

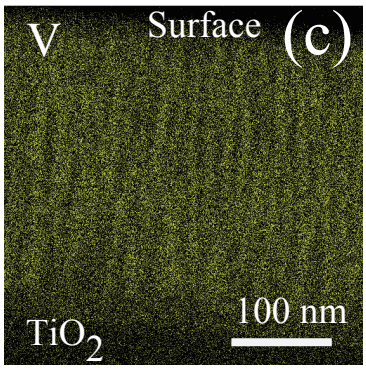

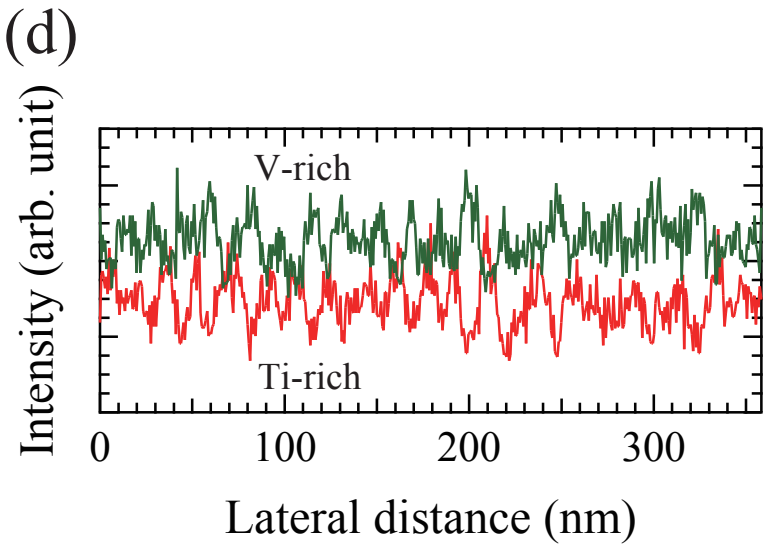

Figs. 5(a)(b)(c)(d). Y. Muraoka et al.

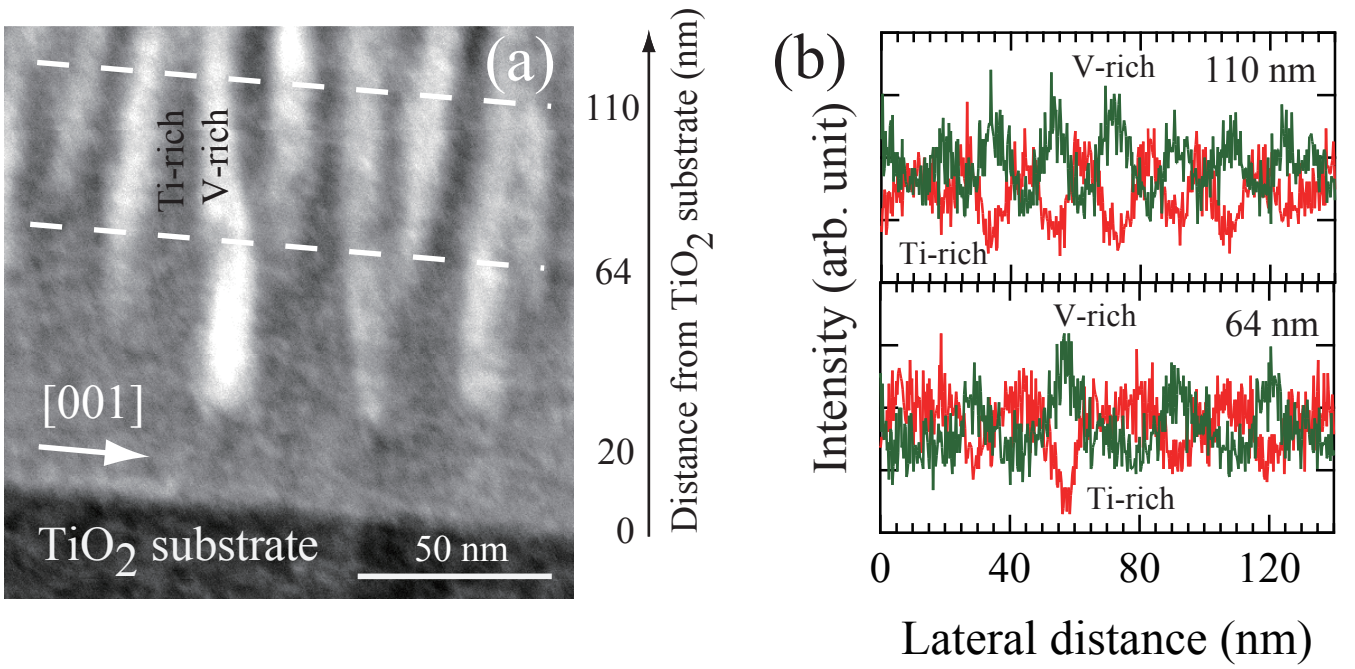

Figs. 6(a)(b). Y. Muraoka et al.

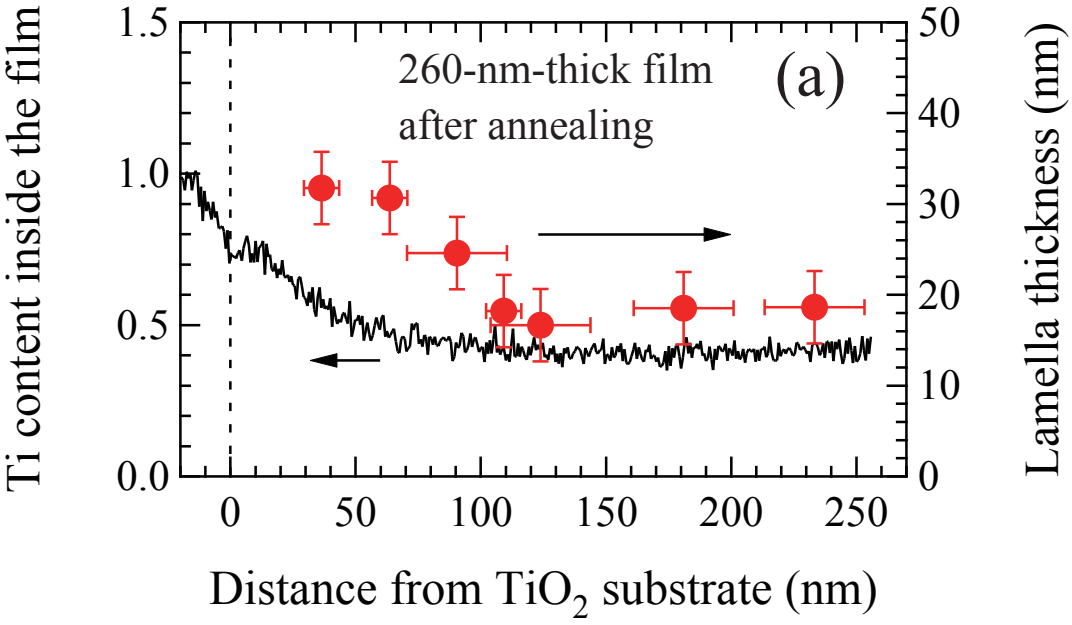

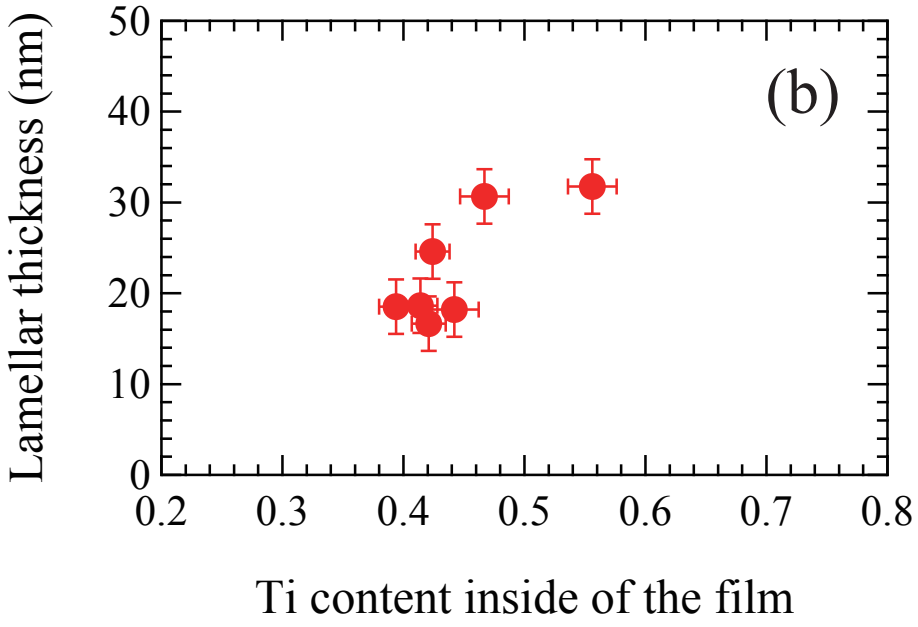

Figs. 7(a)(b). Y. Muraoka et al.

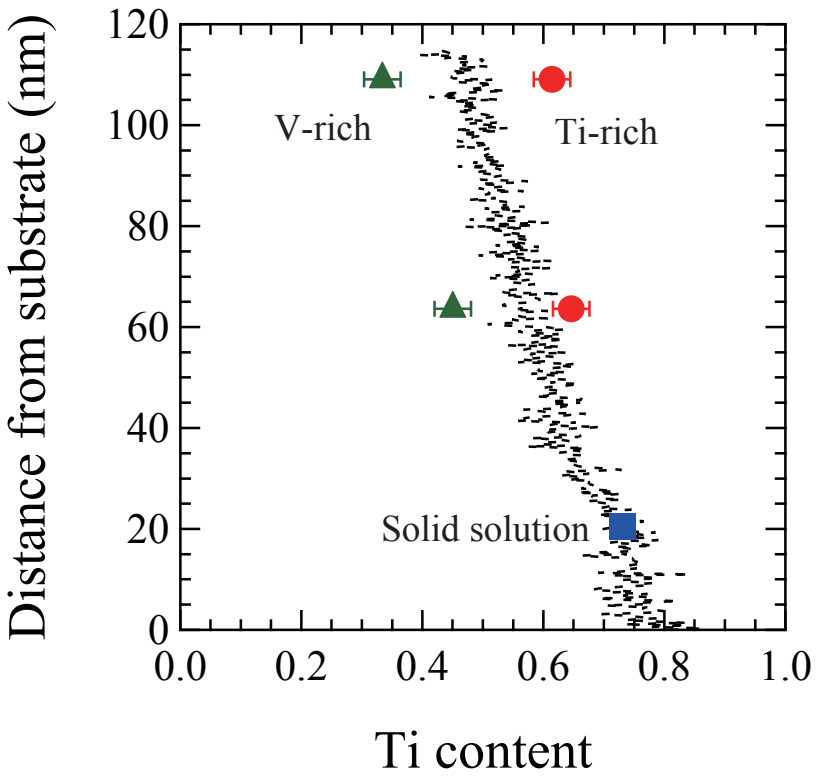

Fig. 8. Y. Muraoka et al.

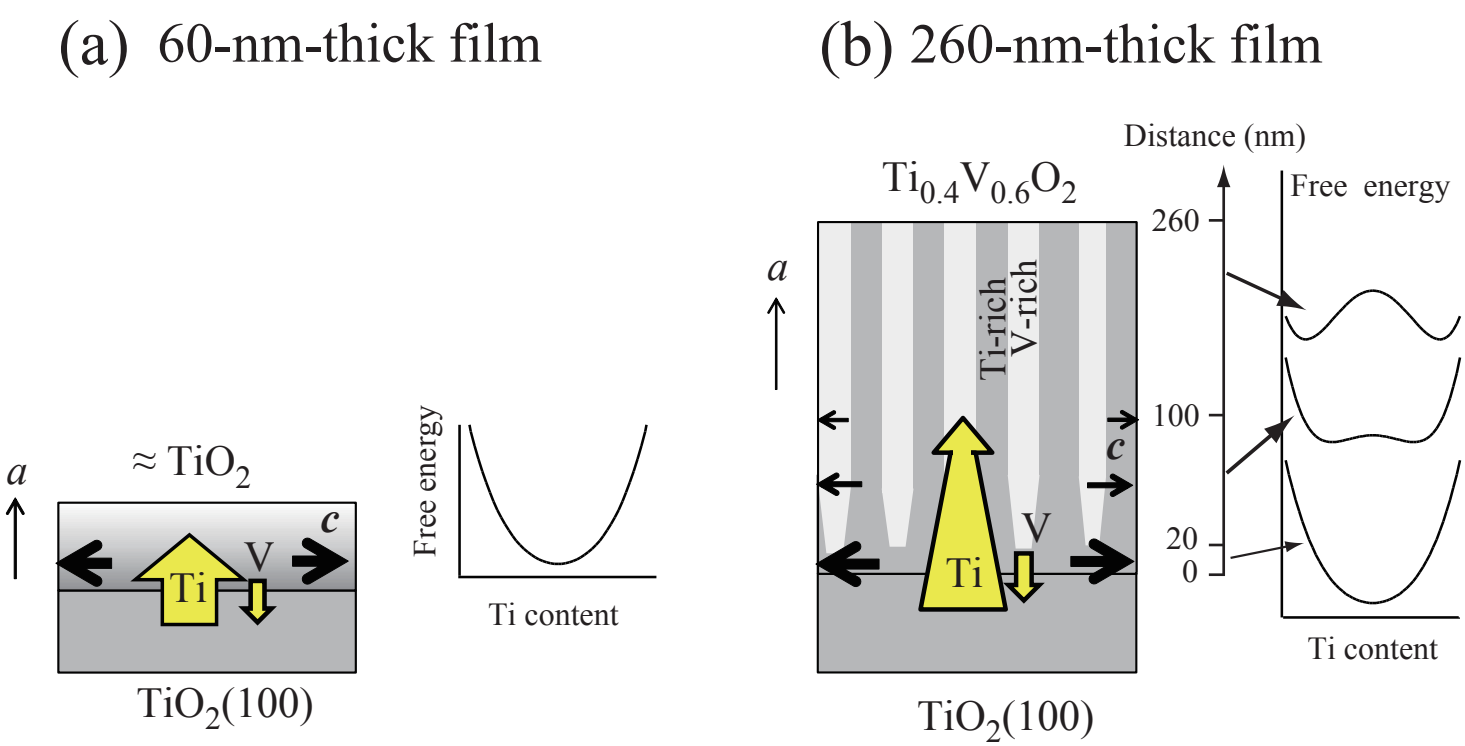

Figs. 9(a)(b). Y. Muraoka et al.

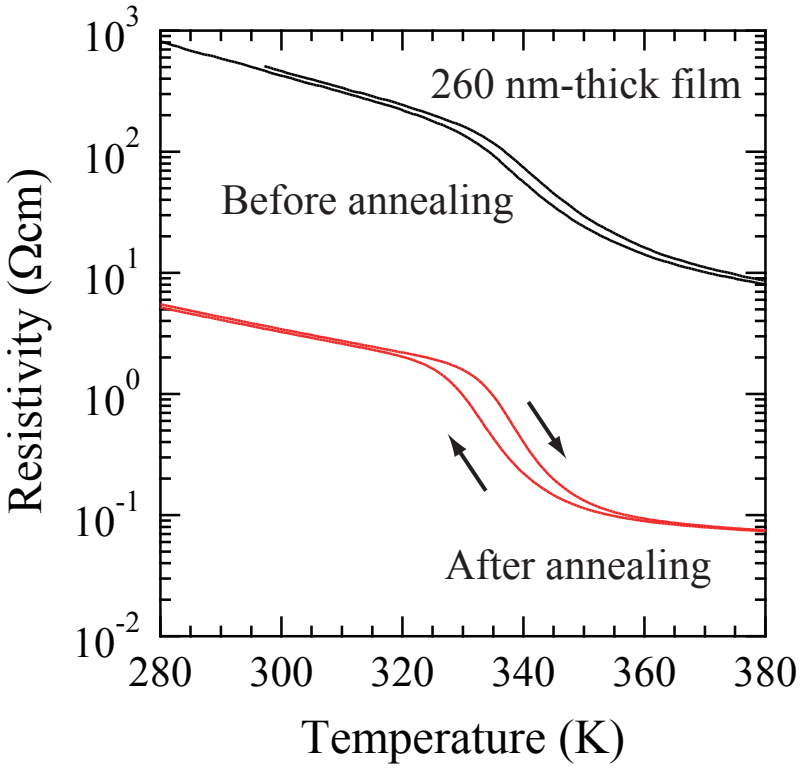

Fig. A.1. Y. Muraoka et al.

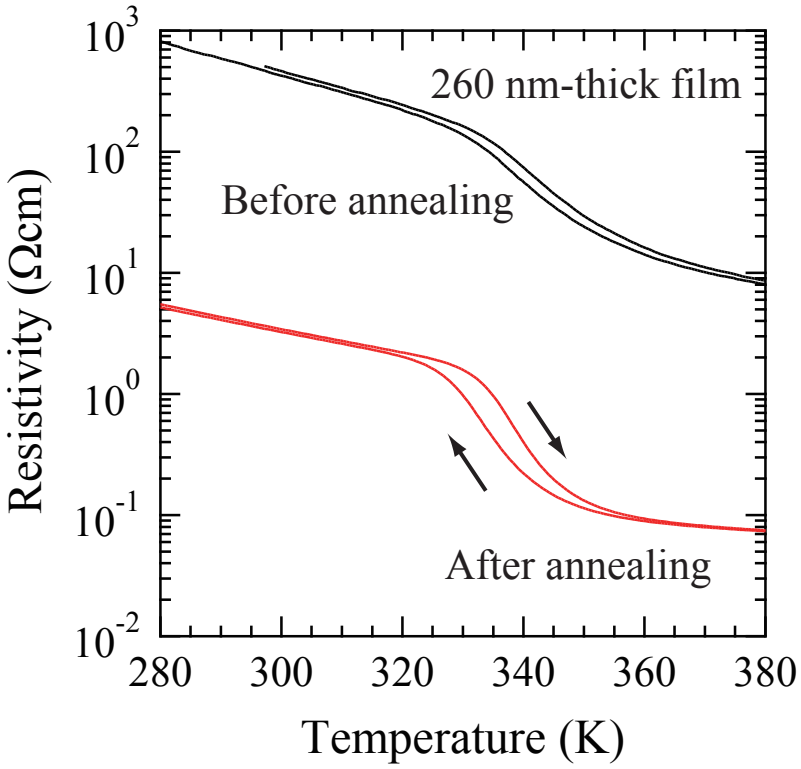

Fig. A.1. Y. Muraoka et al.